Tip-enhanced secondary emission of a semiconductor quantum dot

I. D. Rukhlenko,* A. V. Fedorov, and A. V. Baranov
Saint-Petersburg State University of Information Technologies, Mechanics and Optics, 49 Kronverksky Avenue, 197101 St. Petersburg, Russia

T. S. Perova
Department of Electronic and Electrical Engineering, Trinity College, University of Dublin, Dublin 2, Ireland

K. Berwick
Department of Electronic and Communications Engineering, Dublin Institute of Technology, Dublin 8, Ireland
(Received 12 September 2007; revised manuscript received 23 November 2007; published 30 January 2008)

We present a theoretical study of the luminescence enhancement in a semiconductor quantum dot in the near field of a metallic tip. The electric near field induced by a plane electromagnetic wave near the apex of the perfectly conducting conical tip has been calculated analytically. The results obtained have been used to evaluate the interband matrix element which determines the electron-hole pair generation rate and luminescence intensity of a semiconductor quantum dot. Secondary emission calculations have been carried out using a reduced density matrix approach assuming a radiation frequency close to resonance with the quantum dot fundamental transition. In order to establish the most favorable experimental conditions, we have analyzed the dependence of the interband matrix element and luminescence spectra intensity on the quantum dot size and the distance between the quantum dot and the tip apex. It has been demonstrated that the presence of the metallic tip results in a significant enhancement of the luminescence intensity and leads to a partial violation of the standard selection rules.

DOI: 10.1103/PhysRevB.77.045331 PACS number(s): 78.66.Fd, 63.22.−m, 71.35.Cc, 78.55.Cr

I. INTRODUCTION

One of the most important methods for nanostructure investigation is scanning near-field optical microscopy.[1,2] When combined with modern spectral devices, this method enables one to obtain secondary emission spectra with both high spatial and spectral resolution for single nano-objects. In order to maximize secondary emission excitation efficiency, apertureless scanning devices based on local electromagnetic field enhancement near the metallic tip apex are particularly attractive.[3–5]

The spatial resolution of these methods is principally determined by the apex curvature of the tip and can be as low as several nanometers. Resolutions of below 10 nm are possible using apertureless near-field optical microscopes.[6–11] The ability to obtain secondary emission spectra at such high resolutions enables new techniques for the study of nano-object relaxation parameters, as well as their electron and phonon structure. For example, selective excitation of a single quantum dot (QD) in an ensemble directly provides data on the dynamics of QD transitions. It also eliminates the need to extract the data from the inhomogeneously broadened spectra. In order to interpret the spectroscopic data, it is necessary to have an adequate theoretical description of the secondary emission process from a single nano-object in the presence of the metallic tip. In particular, it is essential to know the optimal conditions of nano-object electronic subsystem excitation and the local-field enhancement effect on the shape and intensity of the luminescence spectra. To the best of our knowledge, despite the importance of the problem, this has not been done to date.

It is well known that optical field enhancement in the vicinity of sharp edges and wedges on metallic bodies occurs for two reasons. These are the resonant excitation of surface plasmons[5,12–14] and the electrostatic lightning-rod effect caused by the geometrical singularity at the surface.[3,15,16] Local-field strength enhancement near the tip apex is of central importance for the realization of high spatial resolution in both Raman[17,18] and luminescence[19] spectroscopies, as well as for effective excitation of various nonlinear processes.[9,20,21]

Currently, a number of numerical methods to compute the electric field strength in the vicinity of an arbitrary tip surface are used. The most popular of these approaches are multiple multipole,[22–25] Green's function,[26] and finite-difference time-domain[17,27,28] methods. These numerical techniques are used when the tip shape excludes the possibility of an analytical solution[26] and only for calculation of the electric field strength.[28–31] Strictly analytical solutions for the corresponding electrodynamic problems are rare, even for tips with relatively simple surfaces. In the literature devoted to these problems, a highly simplified tip model is used,[16,20,21,32] or artificial assumptions are made regarding the tip symmetry.[15,33] Another approach neglects the effect of retardation, solving the Laplace equation.[34–36] All these simplified approaches produce solutions with limited validity. In this work, the calculation of the electric near field of a peg-shaped metallic tip is based on an analytical solution of the associated electrodynamic boundary-value problem.

Using the numerical methods described earlier, the problem of determining the maximal field enhancement of optical radiation at the apex of sharp nano-tips has been intensively studied. As a result, both the tip and incident radiation parameters which maximize the electric field enhancement factor have been unambiguously determined.[16,28–30] However, the secondary emission intensity of a single nano-object

placed near the apex of a nano tip was not considered in detail. Intuitively, it should depend on the nano-object size and geometry as well as on the spatial distribution of the electric field.

The aim of this paper is to analyze the effect of the electric near-field structure on the secondary emission intensity of a single nano-object. We use a semiconductor QD as a representative nano-object, since it is of both practical and fundamental interest.[37–39] In our model, it is assumed that the QD is located near a metallic cone illuminated by a plane electromagnetic wave polarized along the cone's axis. As expected, the calculation shows that, in the immediate vicinity of the cone apex, some of the electric field strength components can exceed the plane wave strength by over an order of magnitude. The calculated near field was used to determine the interband matrix element, which determines the electron-hole pair generation rate and luminescent intensity of a single QD. The QD luminescent intensity was calculated using a reduced density matrix approach with the irradiating field frequency close to resonance with the QD fundamental transition.

An analysis of the dependence of the QD electron-hole pair generation rate on tip size and distance between the QD and tip apex reveals a number of new features which are apparent in the luminescence spectra. These are the following: (i) The maximum electron-hole pair generation rate for transitions between states with the same envelope functions occurs at a nonzero distance between the dot and the tip apex. (ii) For some transitions, the indicated maximum is preceded by the minimum, that is, the generation rate is lower than it would be if the tip was absent. (iii) When the QD surface is in contact with the tip, the electron-hole pair generation rate for dipole-forbidden transitions may exceed that for dipole-allowed transitions by an order of magnitude. (iv) As well depending on the cone and incident plane wave parameters, the generation rate also strongly depends on the QD size. By modeling the luminescence spectra, it has been demonstrated that the presence of the metallic tip results in both an intensity enhancement and a significant spectral shape modification.

This paper is organized as follows. In Sec. II, we present analytical expressions for the electric near-field strength of a perfectly conducting finite cone and estimate the field enhancement factor. In Sec. III, we derive the matrix element of the QD interband transition and analyze the QD electron-hole pair generation rate enhancement due to the presence of the metallic tip. Finally, in Sec. IV, we consider the process of QD luminescence. Here, an expression for the differential cross section of the secondary emission intensity is presented and analyzed.

II. ELECTRIC NEAR-FIELD OF A PERFECTLY CONDUCTING FINITE CONE ILLUMINATED BY A PLANE ELECTROMAGNETIC WAVE

Typically, tips of practical interest are usually modeled by cones. Therefore, without loss of generality, we consider a plane electromagnetic wave of frequency ω illuminating a perfectly conducting metallic cone of interior half angle ϑ_c.

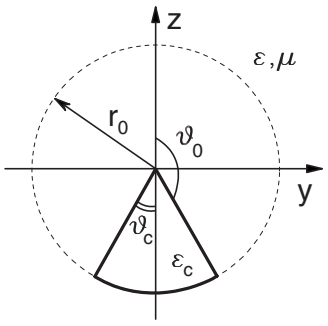

FIG. 1. Perfectly conducting metallic cone with permittivity $\epsilon_c = -\infty$. r_0 is the radius of the spherical base of cone, and ϑ_c is the cone half angle.

Let the cone apex be at the origin of a spherical coordinate system, the cone flank is specified by the inequalities $0 \leqslant r \leqslant r_0$, $\vartheta = \vartheta_0$, and $0 \leqslant \varphi < 2\pi$, where $\vartheta_0 = \pi - \vartheta_c$ and the cone base is considered to be part of a sphere of radius r_0 centered at the origin (Fig. 1). Neglecting the finite radius of curvature of the cone apex, which, at any rate, exceeds the atomic radius, allows us to estimate the maximum value of the field enhancement. Note that assuming the tip to have perfect conductivity will lead to some overestimation of the field enhancement. Despite this, all our general deductions remain valid.

As a first step for further calculations, we are interested in the electric near field inside the sphere of radius r_0 outside the cone. Solving the system of Maxwell's equations in a linear, homogeneous, and source-free medium together with classical boundary conditions, one may show[40] that in the region $0 \leqslant r \leqslant r_0$, $0 \leqslant \vartheta \leqslant \vartheta_0$, $0 \leqslant \varphi < 2\pi$, the electric field vector has the following form:

$$\mathbf{E}(\mathbf{r},t) = \mathbf{E}(\mathbf{r})e^{i\omega t} + \text{c.c.}, \tag{1}$$

where $\mathbf{E}(\mathbf{r}) = E_r\mathbf{e}_r + E_\vartheta\mathbf{e}_\vartheta + E_\varphi\mathbf{e}_\varphi$ is the complex amplitude of the electric field,

$$E_r(r,\vartheta,\varphi) = \sum_{m=-\infty}^{+\infty} \sum_{\sigma} \sigma(\sigma+1) a_{\sigma m} \frac{j_\sigma(\kappa r)}{\kappa r} Y_{\sigma m}(\vartheta,\varphi), \tag{2}$$

$$E_\vartheta(r,\vartheta,\varphi) = \sum_{m=-\infty}^{+\infty} \left(\sum_{\sigma} a_{\sigma m} D_\sigma(\kappa r) \frac{\partial Y_{\sigma m}(\vartheta,\varphi)}{\partial \vartheta} + \sum_{\tau} b_{\tau m} j_\tau(\kappa r) \frac{m}{\sin\vartheta} Y_{\tau m}(\vartheta,\varphi) \right), \tag{3}$$

$$E_\varphi(r,\vartheta,\varphi) = i \sum_{m=-\infty}^{+\infty} \left(\sum_{\sigma} a_{\sigma m} D_\sigma(\kappa r) \frac{m}{\sin\vartheta} Y_{\sigma m}(\vartheta,\varphi) + \sum_{\tau} b_{\tau m} j_\tau(\kappa r) \frac{\partial Y_{\tau m}(\vartheta,\varphi)}{\partial \vartheta} \right), \tag{4}$$

$\kappa = (\omega/c)\sqrt{\epsilon\mu}$, c is the speed of light in vacuum, ϵ and μ are the permittivity and the permeability of the cone surroundings, respectively,

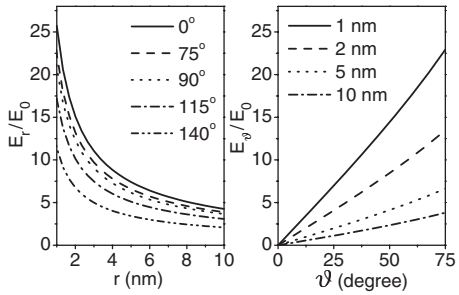

FIG. 2. Left panel: Electric field radial component enhancement $E_r(r,\vartheta,0)/E_0$ for different polar angles ϑ. Right panel: Electric field polar component enhancement $E_\vartheta(r,\vartheta,0)/E_0$ for different distances r. E_0 is the plane wave electric field strength. $\vartheta_c=15°$. For other parameters, see the text.

$$D_\nu(\rho) = (\nu+1)\frac{j_\nu(\rho)}{\rho} - j_{\nu+1}(\rho),$$

$$Y_{\nu m}(\vartheta,\varphi) = \frac{P_\nu^m(\cos\vartheta)}{\sqrt{\Lambda_{\nu m}}}\frac{e^{im\varphi}}{\sqrt{2\pi}},$$

$$\Lambda_{\nu m} = \int_{\cos\vartheta_0}^{1} [P_\nu^m(x)]^2 dx,$$

$j_\nu(\rho)$ is the spherical Bessel function, and $P_\nu^m(x)$ is the Legendre function of the first kind. The constants $a_{\sigma m}$ and $b_{\tau m}$ depend on the cone dimensions, as well as on the plane wave characteristics (see Appendix A). The eigenvalues $\sigma \equiv \sigma_i^m = \sigma_i^{-m}$ $(i=1,2,3,\ldots)$ belong to the Dirichlet condition, and the eigenvalues $\tau \equiv \tau_i^m = \tau_i^{-m}$ belong to the Neumann condition. These conditions result from the constant potential at the cone surface and have the form

$$P_\sigma^m(\cos\vartheta_0) = 0, \qquad \left.\frac{dP_\tau^m(\cos\vartheta)}{d\vartheta}\right|_{\vartheta=\vartheta_0} = 0.$$

To illustrate the local-field enhancement, we consider a metallic cone of apex half angle $\vartheta_c=15°$ and height $r_0=500$ nm located in air. The plane wave with frequency $\omega=2.13\times10^{15}$ s^{-1} ($\hbar\omega=1.4$ eV) irradiating the cone travels in the $-y$ direction and is polarized in the z direction. Figure 2 shows the strengthening of both the radial and polar electric field components near the cone apex for the parameters listed above. From Eq. (1), in order to determine these components, the magnitudes of the complex expressions (2) and (3) are calculated. Clearly, the electric field strength near the cone apex may exceed that of the plane wave (E_0) by in excess of an order of magnitude. In the case considered, the dependence of the functions $E_r(r,\vartheta,\varphi)$ and $E_\vartheta(r,\vartheta,\varphi)$ on the azimuth angle is weak, and so the curves depicted in Fig. 2 for $\varphi=0$ have nearly the same shape for other values of φ. The azimuth electric field component $E_\varphi(r,\vartheta,\varphi)$ is not presented in Fig. 2 since for $r\lesssim10$ nm, this component is smaller than the radial component by 2 orders of magnitude. This implies that the electric near field is essentially axially symmetric near the apex.

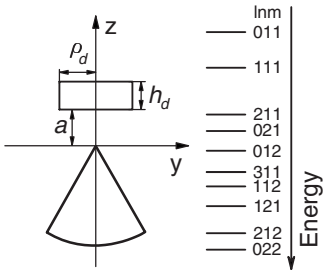

FIG. 3. Cylindrically symmetric QD in the near field of a metallic tip. a is the distance between the QD and tip apex, and h_d and ρ_d are the height and radius of the QD. The order of the energy levels in the valence band of the QD with $\rho_d=h_d$ is shown on the right. Each level is characterized by quantum numbers l, n, and m. A strong confinement limit is assumed.

III. ELECTRON-HOLE PAIR GENERATION IN A SEMICONDUCTOR QUANTUM DOT

In order to study the influence of near-field enhancement on the electron-hole pair generation rate, we consider a cylindrically symmetric quantum dot of radius ρ_d and height h_d located in air at a distance a from the metallic tip apex (Fig. 3). The QD symmetry axis is assumed to be in the z direction. The interaction of QD carriers with the electric field of the plane wave enhanced by the tip leads to electron-hole pair generation. Using a linear approximation, the interaction of the QD electronic subsystem with the electric near field can be represented as[41]

$$\hat{V}(\mathbf{r}) = -\frac{e}{m_0 c}\mathbf{A}(\mathbf{r})\hat{\mathbf{p}}, \tag{5}$$

where e is the electron charge, m_0 is the mass of a free electron, $\mathbf{A}(\mathbf{r})=(i/\kappa\epsilon_d)\mathbf{E}(\mathbf{r})$ is the vector potential within the QD, ϵ_d is the QD permittivity, and $\hat{\mathbf{p}}=-i\hbar\nabla$ is the momentum operator. For simplicity's sake, we assume that the QD and substrate do not affect the magnitude and spatial distribution of the electric near field. Since we are modeling a QD in air, we utilize a potential well with impenetrable boundaries. In the strong confinement limit,[42] the normalized wave functions of electrons (holes) inside the well are characterized by the set of quantum numbers $\nu=\{l,n,m\}$ and are given by[41]

$$|\nu\rangle = \sqrt{\frac{2}{\pi h_d \rho_d^2}}\frac{J_l(\zeta_{ln}\rho/\rho_d)}{J_{l+1}(\zeta_{ln})}\sin\left(\frac{\pi m}{h_d}(z-a)\right)e^{il\varphi}, \tag{6}$$

where ζ_{ln} is the nth root of the lth order cylindrical Bessel function of the first kind, $\rho=r\sin\vartheta$, and $z=r\cos\vartheta$.

It is straightforward to show that[43] in the effective mass approximation for a two-band model of semiconductors with T_d or O_h symmetry, the squared matrix element of the one-photon transition $|i\rangle\rangle \rightarrow |f\rangle\rangle$ is determined by the following expression:

$$V_{\nu_i}^{\nu_f}(\omega) = Av_i \sum_f |\langle\langle f|\hat{V}(\mathbf{r})|i\rangle\rangle|^2 = \varpi(l)\frac{E_p}{m_0}\left(\frac{2e}{\epsilon_d \omega}\right)^2 M_{\nu_i}^{\nu_f}(\omega). \tag{7}$$

Here, Av_i stands for averaging by degenerate initial states, $|f\rangle\rangle = |c\rangle|\nu_f\rangle$ and $|i\rangle\rangle = |v\rangle|\nu_i\rangle$ are the full wave functions of the final and initial electronic states, $|v\rangle$ and $|c\rangle$ are the Bloch functions, $\nu_f = \{l,n,m\}$ and $\nu_i = \{l',n',m'\}$ are the sets of quantum numbers corresponding to the envelope functions $|\nu_f\rangle$ and $|\nu_i\rangle$, $\varpi(l)=1$ for $l=0$ and $\varpi(l)=2$ otherwise, $E_p = m_0 P^2/(2\hbar^2)$, $P = \hbar^2/m_0\langle S|\partial/\partial z|Z\rangle$ is the Kein's parameter,

$$M_{\nu_i}^{\nu_f}(\omega) = \sum_{j=x,y,z} |\langle \nu_f|E_j|\nu_i\rangle|^2, \tag{8}$$

and E_j is the electric field vector projection on to the crystallographic axis j. We consider the plane wave incidence angles ϑ_i and φ_i to be from the positive direction of the crystallographic axes z and x. Using this model, when the interaction is evaluated using Eq. (6), the function $M_{l'n'm'}^{lnm}(\omega)$ becomes

$$M_{l'n'm'}^{lnm}(\omega) = \frac{4}{\pi}(|S_{l-l'+1} + L_{l-l'+1}|^2 + |S_{l-l'-1} - L_{l-l'-1}|^2 + 2|N_{l-l'}|^2). \tag{9}$$

The functions S_q, L_q, and N_q are given in Appendix B.

In the absence of the tip, when transitions in the QD result from the interaction with the plane wave alone, $M_{l'n'm'}^{lnm} = E_0^2 \delta_{ll'}\delta_{nn'}\delta_{mm'}$. Thus, using a dipole approximation, the familiar selection rules are obtained. As a result of these selection rules,[43] dipole-allowed interband transitions occur between states with the same sets of quantum numbers ν_i and ν_f. To a first approximation of the nonstationary perturbation theory, the probability of a direct interband transition with photon absorption is proportional to the function $V_{\nu_i}^{\nu_f}(\omega)$. Because of this, the ratio $M_{lnm}^{lnm}(\omega)/E_0^2$ (for dipole-allowed transitions) characterizes the electron-hole pair generation rate enhancement due to the presence of the metallic tip. In the discussion that follows, this ratio will be referred to as the enhancement function or, more simply, the enhancement of the electron-hole pair generation rate.

Figure 4 presents the enhancement function dependence on the distance between the QD and the tip apex for transitions between states with the same sets of quantum numbers. For this study, unless otherwise specified, we assume that $\omega=1.4$ eV, $\vartheta_c=15°$, $r_0=500$ nm, $\vartheta_i=\varphi_i=\pi/2$, and $s_\vartheta=1$. For all the transitions in Fig. 4, the maximal electron-hole pair generation rate enhancement is observed for QD separations of 1–2 nm from the tip apex. The value of the enhancement is considerably in excess of unity. For some transitions, e.g., 212-212, the maximum of the enhancement function is preceded by a minimum whose value can be far less than unity. This is a consequence of the QD axial symmetry and, as mentioned earlier, the similar symmetry of the electric near field.

Intriguingly, it was found that the maximal value of the enhancement function is very sensitive to QD size. The corresponding dependencies for dipole-allowed transitions are shown in Fig. 5. As is evident from the plots, in QDs of intermediate sizes ($\rho_d = h_d \sim 2.5$–5 nm), the electron-hole pair generation rate can be enhanced by the metallic tip by tens of times, while in smaller QDs ($\rho_d = h_d \sim 1$–2.5 nm), the enhancement may be greater than 2 orders of magnitude.

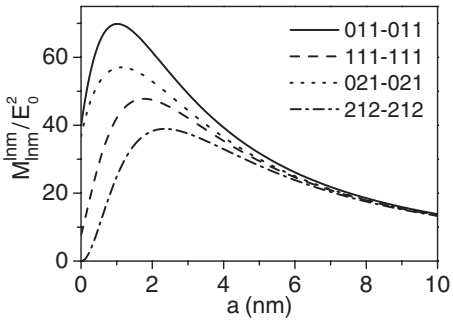

FIG. 4. Dependence of the enhancement function on distance a (see Fig. 3) for dipole-allowed transitions. In the calculations, the following parameters were used: $\rho_d = h_d = 3$ nm, $\vartheta_c = 15°$, $r_0 = 500$ nm, and $\omega = 1.4$ eV. A plane wave travels in the $-y$ direction and is polarized in the z direction.

In the event of transitions between states with different sets of quantum numbers, it is meaningless to speak about the enhancement of the electron-hole pair generation rate since these transitions are forbidden in the dipole approximation. In this instance, the enhancement function will be treated as the ratio of the dipole-forbidden transition rate in the presence of the tip to the rate of the dipole-allowed transition in the absence of the tip. It is obvious that the ratio, thus defined, determines the selection rules. Figure 6 illustrates the ratio $M_{l'n'm'}^{lnm}/E_0^2$ for five transitions between states differing from each other in one of the quantum number sets ν_i and ν_f by 1. Unlike the spectra depicted in Fig. 4, the spectra in Fig. 6 peak at $a=0$. The decrease of the enhancement ratio depends on the quantum number by which the states of the transition differ. The most rapid decrease in this ratio occurs for transitions with ν_i and ν_f differing in m: the value of the ratio drops below unity for QD displacements from the tip apex of approximately 1 nm. This calculation

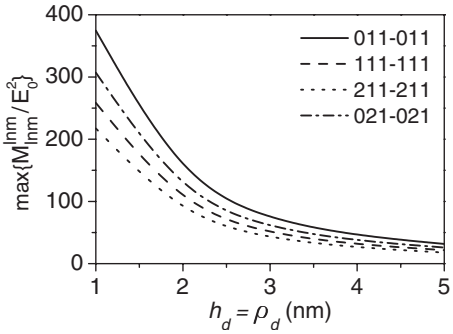

FIG. 5. Dependence of the enhancement function maximum on QD size $h_d = \rho_d$ (see Fig. 3) for dipole-allowed transitions. In these calculations, the following parameters were used: $\vartheta_c = 15°$, $r_0 = 500$ nm, and $\omega = 1.4$ eV. The plane wave travels in the $-y$ direction and is polarized in the z direction.

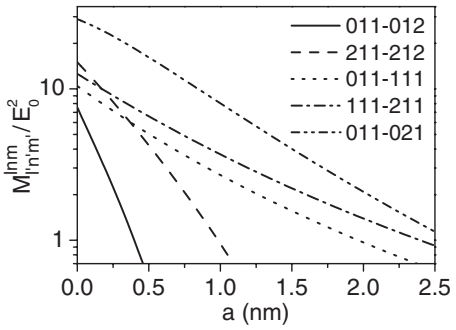

FIG. 6. Dependence of the ratio $M^{lnm}_{l'n'm'}/E_0^2$ on distance a (see Fig. 3) for dipole-forbidden transitions. In these calculations, the following parameters were used: $\rho_d=h_d=3$ nm, $\vartheta_c=15°$, $r_0=500$ nm, and $\omega=1.4$ eV. The plane wave travels in the $-y$ direction and is polarized in the z direction.

shows that if the states involved in the transition differ by unity in two of the quantum numbers, or by 2 in one of the quantum numbers, then the maximal generation rate is also achieved at $a=0$, but is smaller. Thus, we conclude that in the near field of the metallic tip, the standard selection rules are radically modified. This deduction is readily illustrated by Fig. 7 in which the values of the ratio $(M^{lnm}_{l'n'm'}/E_0^2)|_{a=0}$ are shown. One can see that, by convention, all the dipole-forbidden transitions can be divided in two groups. For transitions of the first group, $M^{lnm}_{l'n'm'}/E_0^2>10^{-2}$ and the standard selection rules fail, while for transitions of the second group, $M^{lnm}_{l'n'm'}/E_0^2\leqslant 10^{-7}$ and the selection rules remain valid. The dependence of the $M^{lnm}_{l'n'm'}/E_0^2$ ratio maximum on the QD size is similar to those depicted in Fig. 5. For QDs with $\rho_d=h_d\sim 1-2$ nm, the maximal value of the ratio $M^{lnm}_{l'n'm'}/E_0^2$ may exceed 100.

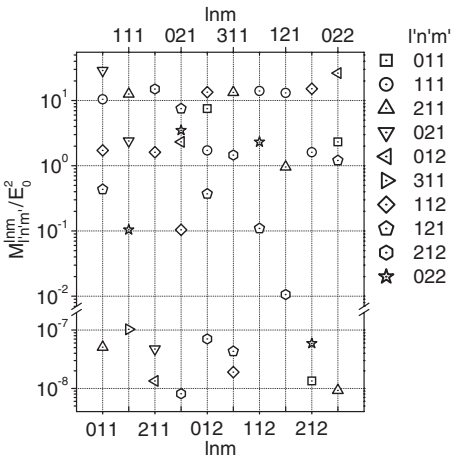

FIG. 7. The ratio $M^{lnm}_{l'n'm'}/E_0^2$ at $a=0$ for dipole-forbidden transitions. We note that $M^{lnm}_{l'n'm'}=M^{l'n'm'}_{lnm}$. Only transitions for which $M^{lnm}_{l'n'm'}/E_0^2>10^{-9}$ are shown. In the calculations, the following parameters were used: $\rho_d=h_d=3$ nm, $\vartheta_c=15°$, $r_0=500$ nm, and $\omega=1.4$ eV. A plane wave travels in the $-y$ direction and is polarized in the z direction.

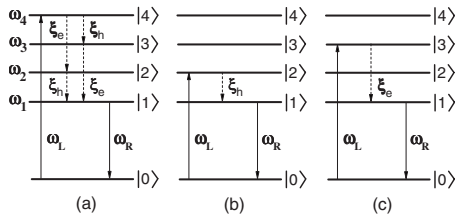

FIG. 8. Scheme of QD energy levels and transitions corresponding to different luminescence processes. ω_L is the local-field frequency, ω_R is the radiation field frequency, and ξ_e and ξ_h are the relaxation rates of electrons and holes, respectively.

IV. QUANTUM DOT SPONTANEOUS SECONDARY EMISSION

The enhancement of the laser field by the metallic tip is apparent in resonant photoluminescence spectra, which contain valuable information on the energy and phase relaxation processes, as well as on the structure of single QD energy spectra.[44–54] The important theoretical problem is to determine the optimum experimental conditions for the maximum luminescence spectra intensity. To solve the problem, we consider the three single secondary emission events illustrated in Fig. 8. Each event consists of the initial resonant generation of an electron-hole pair in a QD excited state by the tip's local field with frequency ω_L (denoted as ω previously). This is followed by intraband relaxation of the electron and/or hole to a ground state with a consequent emission of elementary excitations of the QD and/or its surroundings. The associated spontaneous emission of light with frequency ω_R is due to the annihilation of the electron-hole pair in the ground state.

Let us assume that the photoexcitation of the electron-hole pair, the energy relaxation of the QD electronic subsystem, and the light emission are a unified process. As before, we shall restrict our consideration to a specific type of QD with $\rho_d=h_d$. We shall describe the QD energy states with the two-band model of semiconductors[55] using the electron-hole pair representation. In this case the electron-hole pair energy spectra have the form[41]

$$E^{lnm}_{l'n'm'}=E_g+\frac{\hbar^2}{2h_d^2}\left(\frac{\zeta^2_{l'n'}+\pi^2m'^2}{m_h}+\frac{\zeta^2_{ln}+\pi^2m^2}{m_e}\right), \quad (10)$$

where E_g is the semiconductor band gap, and m_e and m_h are the effective masses of electrons and holes in the QD. Figure 8(a) schematically depicts four lower-energy states of the spectrum (10) provided that $m_h>m_e$: $|1\rangle=|e_{011}h_{011}\rangle$, $|2\rangle=|e_{011}h_{111}\rangle$, $|3\rangle=|e_{111}h_{011}\rangle$, and $|4\rangle=|e_{111}h_{111}\rangle$. The symbol $|0\rangle$ denotes the electron-hole pair vacuum state. According to the previous section, in the near field of the metallic tip, one-photon transitions can take place between the vacuum state $|0\rangle$ and any of the states $|j\rangle$ $(j=1,2,3,4)$.

Suppose that the energy of the tip's local-field quanta is close to resonance with the transition $|0\rangle\rightarrow|4\rangle$, i.e., $\omega_L\approx\omega_4=E^{111}_{111}/\hbar$, and the secondary emission frequency $\omega_R\approx\omega_1=E^{011}_{011}/\hbar$ [Fig. 8(a)]. Using perturbation theory for the reduced density matrix,[56] it can be shown that, in the

rotating-wave approximation under stationary excitation of the QD, the emission rate of photons with frequency ω_R and polarization vector $\mathbf{e}_R$ is given by

$$W^{(4)} = g_R |V_{40}^{(L)}|^2 |V_{01}^{(R)}|^2 \frac{\gamma_{40}}{\Delta_4^2 + \gamma_{40}^2} \frac{\gamma_{10}}{\Delta_R^2 + \gamma_{10}^2} \frac{\xi_e \xi_h}{\gamma_{44}\gamma_{11}} \left(\frac{1}{\gamma_{22}} + \frac{1}{\gamma_{33}} \right), \tag{11}$$

where $|V_{40}^{(L)}|^2 = V_{111}^{111}(\omega_L)$ [see Eq. (7)] and $\Delta_4 = \omega_L - \omega_4$. From here on, we use the following notations: $g_R = 2\pi\omega_R/(\epsilon_d \hbar^3 V)$, V is the normalization volume, $V_{01}^{(R)} = \langle 0|(-e\mathbf{r})\mathbf{e}_R|1\rangle$, $e\mathbf{r}$ is the dipole moment operator, $\Delta_R = \omega_R - \omega_1$, $\gamma_{j0} = \hat{\gamma}_{j0} + \gamma_{jj}/2$ is the full dephasing rate of the transition $|j\rangle \to |0\rangle$, $\hat{\gamma}_{j0}$ is the pure dephasing rate of the transition $|j\rangle \to |0\rangle$, ξ_e and ξ_h are the relaxation rates of electrons and holes, and γ_{jj} is the inverse lifetime of the state $|j\rangle$. For the sake of simplicity in the following discussion, we assume that $\gamma_{44} = \xi_e + \xi_h + \gamma_4$, $\gamma_{33} = \xi_e + \gamma_3$, and $\gamma_{22} = \xi_h + \gamma_2$, where γ_j $(j = 2,3,4)$ accounts for radiation broadening and/or possible nonradiative recombination of the electron-hole pair. It can be shown that in the effective mass approximation for the two-band model of semiconductors with T_d or O_h symmetry, the following equality holds: $|V_{10}^{(R)}|^2 = (2e/\omega_R)^2 E_p/m_0$.

If the energy of the local-field quanta is close to resonance with the transition $|0\rangle \to |2\rangle$, i.e., $\omega_L \approx \omega_2 = E_{111}^{011}/\hbar$ [Fig. 8(b)], then the emission rate of photons with frequency $\omega_R \approx \omega_1$ may be written as

$$W^{(2)} = g_R |V_{20}^{(L)}|^2 |V_{01}^{(R)}|^2 \frac{\gamma_{20}}{\Delta_2^2 + \gamma_{20}^2} \frac{\gamma_{10}}{\Delta_R^2 + \gamma_{10}^2} \frac{\xi_h}{\gamma_{22}\gamma_{11}}, \tag{12}$$

where $|V_{20}^{(L)}|^2 = V_{111}^{011}(\omega_L)$ and $\Delta_2 = \omega_L - \omega_2$. In the case when $\omega_L \approx \omega_3 = E_{011}^{111}/\hbar$ [Fig. 8(c)], the analogous photon emission rate is

$$W^{(3)} = g_R |V_{30}^{(L)}|^2 |V_{01}^{(R)}|^2 \frac{\gamma_{30}}{\Delta_3^2 + \gamma_{30}^2} \frac{\gamma_{10}}{\Delta_R^2 + \gamma_{10}^2} \frac{\xi_e}{\gamma_{33}\gamma_{11}}, \tag{13}$$

where $|V_{30}^{(L)}|^2 = V_{011}^{111}(\omega_L)$, $\Delta_3 = \omega_L - \omega_3$.

In order to allow comparison with data from secondary emission experiments, we need to relate the photon emission rates (11)–(13) to the luminescence differential cross section. According to its definition,[57] the QD luminescence differential cross section $\Theta(\omega_L, \omega_R)$ is the ratio of the spectral density of the QD radiation intensity to the plane wave intensity $I_0 = (c/2\pi)E_0^2$. Using this definition and Eqs. (11)–(13) and (7), one gets

$$\begin{aligned}
\Theta(\omega_L, \omega_R) &\equiv \frac{d^2\sigma}{d\omega_R d\Omega} \\
&= \frac{V}{I_0} \frac{\hbar\omega_R^3}{4\pi^3 c^3} \sum_i W^{(i)}(\omega_L, \omega_R) \\
&= \frac{1}{\pi\epsilon_d^3} \left(\frac{2e}{c} \right)^4 \left(\frac{2E_p}{m_0 \hbar} \frac{\omega_R}{\omega_L} \right)^2 \frac{\gamma_{10}}{\Delta_R^2 + \gamma_{10}^2} \frac{1}{\gamma_{11}} \\
&\quad \times \left[2 \frac{M_{111}^{111}(\omega_L)}{E_0^2} \frac{\gamma_{40}}{\Delta_4^2 + \gamma_{40}^2} \frac{\xi_e \xi_h}{\gamma_{44}} \left(\frac{1}{\gamma_{22}} + \frac{1}{\gamma_{33}} \right) \right.
\end{aligned}$$

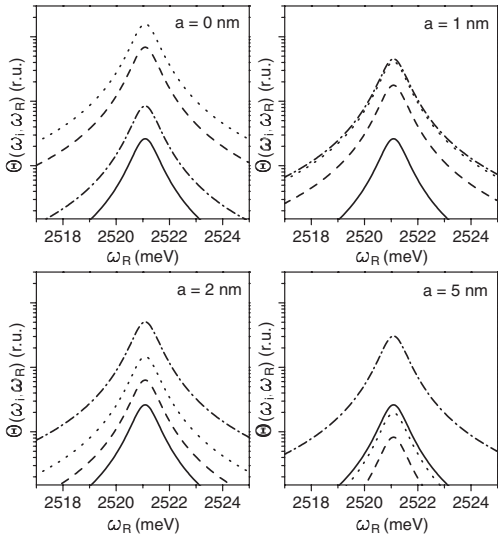

FIG. 9. PL differential cross section spectra $\Theta(\omega_i, \omega_R)$ for different distances a. Solid lines correspond to the $\Theta(\omega_4, \omega_R)$ spectrum of a QD located far from the tip ($a \gg r_0$), dashed lines correspond to $\Theta(\omega_2, \omega_R)$ spectra, dotted lines to $\Theta(\omega_3, \omega_R)$ spectra, and dashed-dotted lines to $\Theta(\omega_4, \omega_R)$ spectra. In these calculations, the following parameters were used: $\rho_d = h_d = 3$ nm, $\vartheta_c = 15°$, and $r_0 = 200$ nm. A plane wave travels in the $-y$ direction and is polarized in the z direction.

$$\left. + 2 \frac{M_{011}^{111}(\omega_L)}{E_0^2} \frac{\gamma_{30}}{\Delta_3^2 + \gamma_{30}^2} \frac{\xi_e}{\gamma_{33}} + \frac{M_{111}^{011}(\omega_L)}{E_0^2} \frac{\gamma_{20}}{\Delta_2^2 + \gamma_{20}^2} \frac{\xi_h}{\gamma_{22}} \right]. \tag{14}$$

This expression describes the differential cross section spectra of both resonant photoluminescence (PL) and photoluminescence excitation (PLE). Its structure indicates that the dependence of the secondary emission intensity on the distance between the QD and the tip as well as on the QD size is governed by the enhancement function $M_{l'n'm'}^{lnm}(\omega_L)/E_0^2$. Apart from the enhancement function, the relative intensities in the spectral maxima are strongly dependent on the relaxation parameters γ_{i0}, γ_{ii} $(i = 2,3,4)$, ξ_e, and ξ_h.

In order to plot the secondary emission spectra $\Theta(\omega_L, \omega_R)$, we consider a GaAs QD with $\rho_d = h_d = 3$ nm. In our calculations, we use $m_e = 0.069m_0$, $m_h = 0.5m_0$, $E_g = 1.428$ eV, $\gamma_4 = \gamma_3 = \gamma_2 = 0.4$ meV, and $\hat{\gamma}_{40} = \hat{\gamma}_{30} = \hat{\gamma}_{20} = 0.5$ meV. The mechanisms of QD carrier relaxation, which are responsible for the rates ξ_e and ξ_h, are extremely varied.[58–66] We shall assume that the QD carrier relaxation is dominated by interaction with the remote plasmon-LO-phonon modes of the doped substrate. In this situation, theoretical estimates predict that[58,59] the carrier relaxation rate may be as great as 10^{10}–10^{11} s^{-1}. So, we use values of $\xi_e = 0.07$ meV and $\xi_h = 0.02$ meV. Figure 9 illustrates the PL differential cross section spectra for both dipole-allowed and dipole-forbidden transitions in the QD exposed to the metallic tip near field. For comparison, the same figure depicts the differential cross section for the transition $|0\rangle \to |4\rangle$, which is resonantly ex-

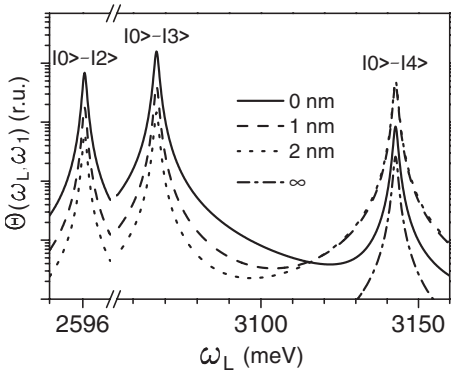

FIG. 10. PLE differential cross section spectra $\Theta(\omega_L, \omega_1)$ for various distances a. Dashed-dotted line shows the cross section for a QD located far from the tip ($a \gg r_0$). In these calculations, the following parameters were used: $\rho_d = h_d = 3$ nm, $\vartheta_c = 15°$, and $r_0 = 200$ nm. A plane wave travels in the $-y$ direction and is polarized in the z direction.

cited by the plane wave in the absence of the tip. From these figures, we notice that for $a=0$, the PL spectrum intensity for the dipole-forbidden transition can exceed that for the dipole-allowed transition by an order of magnitude. For most typical half angles ϑ_c, the enhancement of the spectral intensity for dipole-allowed transitions may reach 2 orders of magnitude. PLE differential cross section spectra are presented in Fig. 10. These spectra also exhibit a rise of the dipole-forbidden transitions in the QD in the vicinity of the tip apex.

V. CONCLUSION

The electric near field of a perfectly conducting conical tip illuminated by a plane electromagnetic wave polarized along the tip axis has been calculated analytically in order to find the matrix element of the induced optical transitions. In the calculations, we have ignored spin degeneracy and assumed that the QD envelope wave functions are determined by an infinite-barrier potential well, while the Bloch wave functions have p symmetry for the triply degenerate valance band and s symmetry for the conduction band. It was found that local field strengthening results in a strong enhancement of the electric dipole transitions, whereas large field gradients lead to drastic modification of the standard selection rules. The results obtained were used for the calculation of photoluminescence differential cross section spectra of cylindrically symmetric semiconductor QDs in the strong confinement limit. Analysis of the spectra revealed that the maximum secondary emission intensity for dipole-allowed transitions takes place for a QD offset several nanometers from the tip, while for dipole-forbidden transitions, it occurs when the QD and the tip are in intimate contact. The strong dependence of the differential cross section spectral intensity on the distance between the QD and the tip apex must be taken into account in highly resolved near-field optical experiments. In future work, it would be interesting to abandon the infinite conductivity assumption to include the effects of surface plasmon resonances in the field enhancement model.

ACKNOWLEDGMENT

Three of the authors (I.D.R., A.V.F., and A.V.B.) are grateful to the RFBR (Grants No. 06-02-17036a and No. 05-02-16212a) for partial financial support of this work.

APPENDIX A

The application of the well-known boundary and continuity conditions for the electromagnetic field[40] leads to the following expressions for the multipole coefficients $a_{\sigma m}$ and $b_{\tau m}$:

$$a_{\sigma m} = \frac{1}{j_\sigma(\rho_0)\sigma(\sigma+1)} \sum_{n=m}^{\infty} (a_{nm}^{inc} j_n(\rho_0) + a_{nm}^{sc} h_n^{(2)}(\rho_0)) X_{nm}^{\sigma},$$

$$b_{\tau m} = \frac{1}{D_\tau(\rho_0)\tau(\tau+1)} \sum_{n=m}^{\infty} [-(a_{nm}^{inc} j_n(\rho_0) + a_{nm}^{sc} h_n^{(2)}(\rho_0)) \xi_{nm}^{\tau} + (b_{nm}^{inc} D_n(\rho_0) + b_{nm}^{sc} D_n^{(2)}(\rho_0)) X_{nm}^{\tau}],$$

where $\rho_0 = \kappa r_0$,

$$X_{nm}^{\sigma} = \frac{n(n+1)}{n(n+1) - \sigma(\sigma+1)} \frac{P_n^m(\cos\vartheta_0) Q_\sigma^m(\cos\vartheta_0)}{\sqrt{\Lambda_{\sigma m}\Lambda_{nm}}},$$

$$X_{nm}^{\tau} = \frac{\tau(\tau+1)}{\tau(\tau+1) - n(n+1)} \frac{P_\tau^m(\cos\vartheta_0) Q_n^m(\cos\vartheta_0)}{\sqrt{\Lambda_{\tau m}\Lambda_{nm}}},$$

$$\xi_{nm}^{\tau} = m \frac{P_n^m(\cos\vartheta_0) P_\tau^m(\cos\vartheta_0)}{\sqrt{\Lambda_{\tau m}\Lambda_{nm}}},$$

$$D_\nu^{(2)}(\rho) = (\nu+1)\frac{h_\nu^{(2)}(\rho)}{\rho} - h_{\nu+1}^{(2)}(\rho),$$

$$Q_\nu^m(u) = (\nu - m + 1) P_{\nu+1}^m(u) - (\nu+1) u P_\nu^m(u),$$

and $h_\nu^{(2)}(\rho)$ is the spherical Hankel function of the second kind. The coefficients a_{nm}^{inc} and b_{nm}^{inc} are the multipole amplitudes of the incident plane wave. If the wave propagation is determined by angles ϑ_i and φ_i while the unit polarization vector has the form $\mathbf{s} = s_\vartheta \mathbf{e}_\vartheta + s_\varphi \mathbf{e}_\varphi$, then[40,67]

$$a_{nm}^{inc} = \alpha_{nm} \frac{s_\vartheta Q_n^m(\cos\vartheta_i) + i m s_\varphi P_n^m(\cos\vartheta_i)}{\sin\vartheta_i} e^{im\varphi_i},$$

$$b_{nm}^{inc} = \alpha_{nm} \frac{s_\varphi Q_n^m(\cos\vartheta_i) - i m s_\vartheta P_n^m(\cos\vartheta_i)}{\sin\vartheta_i} e^{im\varphi_i},$$

where

$$\alpha_{nm} = E_0 \frac{4\pi i^{n+1}}{n(n+1)} \sqrt{\frac{2n+1}{4\pi}\frac{(n-m)!}{(n+m)!}}, \quad n \geqslant 1,$$

$\alpha_{0m} = 0$, and E_0 is the plane wave electric field strength. Using the expressions for $a_{\sigma m}$ and $b_{\tau m}$ in the boundary condition and continuity-condition for the transverse part of the electric field on the sphere $r = r_0$, one may show that, for

specified m, the scattering coefficients a_{nm}^{sc} and b_{nm}^{sc} can be found by solving the following infinite system of linear equations:

$$\sum_{k=n}^{\infty} M_{nk} x_k = y_n,$$

in which $x_k = (\ldots, a_{km}^{sc}, \ldots, \ldots, b_{km}^{sc}, \ldots)$, $y_n = (\ldots, c_{nm}^{inc}, \ldots, \ldots, d_{nm}^{inc}, \ldots)$,

$$M_{nk} = \left(\begin{array}{c|c} A_{nk}^{(1)} & B_{nk}^{(1)} \\ \hline A_{nk}^{(2)} & B_{nk}^{(2)} \end{array} \right),$$

$$c_{nm}^{inc} = a_{nm}^{inc} D_n(\rho_0) n(n+1) - \sum_{k=m}^{\infty} (a_{km}^{inc} j_k(\rho_0)(\Psi_{nm}^k + \Phi_{nm}^k) - b_{km}^{inc} D_k(\rho_0) \Gamma_{nm}^k),$$

$$d_{nm}^{inc} = b_{nm}^{inc} j_n(\rho_0) n(n+1) + \sum_{k=m}^{\infty} (a_{km}^{inc} j_k(\rho_0) \gamma_{nm}^k - b_{km}^{inc} D_k(\rho_0) \chi_{nm}^k),$$

$$A_{nk}^{(1)} = h_k^{(2)}(\rho_0)(\Psi_{nm}^k + \Phi_{nm}^k) - D_n^{(2)}(\rho_0) n(n+1) \delta_{nk},$$

$$B_{nk}^{(1)} = - D_k^{(2)}(\rho_0) \Gamma_{nm}^k,$$

$$A_{nk}^{(2)} = - h_k^{(2)}(\rho_0) \gamma_{nm}^k,$$

$$B_{nk}^{(2)} = D_k^{(2)}(\rho_0) \chi_{nm}^k - h_n^{(2)}(\rho_0) n(n+1) \delta_{nk},$$

$$\Psi_{nm}^k = \sum_{\sigma} \frac{X_{km}^{\sigma} X_{nm}^{\sigma}}{\sigma(\sigma+1)} \frac{D_{\sigma}(\rho_0)}{j_{\sigma}(\rho_0)},$$

$$\Phi_{nm}^k = \sum_{\tau} \frac{\xi_{km}^{\tau} \xi_{nm}^{\tau}}{\tau(\tau+1)} \frac{j_{\tau}(\rho_0)}{D_{\tau}(\rho_0)},$$

$$\Gamma_{nm}^k = \sum_{\tau} \frac{X_{km}^{\tau} \xi_{nm}^{\tau}}{\tau(\tau+1)} \frac{j_{\tau}(\rho_0)}{D_{\tau}(\rho_0)},$$

$$\gamma_{nm}^k = \sum_{\tau} \frac{X_{nm}^{\tau} \xi_{km}^{\tau}}{\tau(\tau+1)} \frac{j_{\tau}(\rho_0)}{D_{\tau}(\rho_0)},$$

$$\chi_{nm}^k = \sum_{\tau} \frac{X_{km}^{\tau} X_{nm}^{\tau}}{\tau(\tau+1)} \frac{j_{\tau}(\rho_0)}{D_{\tau}(\rho_0)}.$$

APPENDIX B

In order to perform the explicit calculation of $M_{\nu_i}^{\nu_f}(\omega)$ defined in Eq. (8), we note that for the angles ϑ_i and φ_i, measured from the positive direction of the crystallographic axes z and x, we have

$$E_x = E_r \sin\vartheta \cos\varphi + E_{\vartheta} \cos\vartheta \cos\varphi - E_{\varphi} \sin\varphi,$$

$$E_y = E_r \sin\vartheta \sin\varphi + E_{\vartheta} \cos\vartheta \sin\varphi + E_{\varphi} \cos\varphi,$$

$$E_z = E_r \cos\vartheta - E_{\vartheta} \sin\vartheta.$$

Substituting these expressions into Eq. (8) and noting that

$$\sin\vartheta = \frac{\rho}{\sqrt{\rho^2 + z^2}}, \quad \cos\vartheta = \frac{z}{\sqrt{\rho^2 + z^2}},$$

we perform the corresponding integrations over the quantum dot volume using cylindrical coordinates. After some algebra, we obtain Eq. (9) with

$$S_q = \sum_{\sigma} a_{\sigma q} [\sigma(\sigma+1) I_{\sigma q}^{(1)} + I_{\sigma q}^{(2)}] + q \sum_{\tau} b_{\tau q} I_{\tau q}^{(3)},$$

$$L_q = q \sum_{\sigma} a_{\sigma q} I_{\sigma q}^{(4)} + \sum_{\tau} b_{\tau q} I_{\tau q}^{(5)},$$

$$N_q = \sum_{\sigma} a_{\sigma q} [\sigma(\sigma+1) I_{\sigma q}^{(6)} + I_{\sigma q}^{(7)}] + q \sum_{\tau} b_{\tau q} I_{\tau q}^{(8)}.$$

Here,

$$I_{\alpha q}^{(i)} = \int_0^1 \int_0^1 \Upsilon_{\alpha q}^{(i)}(x,y) \Xi_{l'n'm'}^{lnm}(x,y) x dx dy,$$

$$\Xi_{l'n'm'}^{lnm}(x,y) = \frac{J_{l'}(\zeta_{l'n'} x) J_l(\zeta_{ln} x)}{J_{l'+1}(\zeta_{l'n'}) J_{l+1}(\zeta_{ln})} \sin(\pi m y) \sin(\pi m' y),$$

where the functions $\Upsilon_{\alpha q}^{(i)}(x,y)$ are defined as

$$\Upsilon_{\sigma q}^{(1)}(x,y) = \frac{S(x,y)}{C(x,y)} \Upsilon_{\sigma q}^{(6)}(x,y),$$

$$\Upsilon_{\sigma q}^{(2)}(x,y) = \frac{C(x,y)}{S(x,y)} \Upsilon_{\sigma q}^{(7)}(x,y),$$

$$\Upsilon_{\tau q}^{(3)}(x,y) = \frac{C(x,y)}{S(x,y)} \Upsilon_{\tau q}^{(8)}(x,y),$$

$$\Upsilon_{\sigma q}^{(4)}(x,y) = \frac{D_{\sigma}[\kappa R(x,y)]}{S(x,y)} \frac{P_{\sigma}^q[C(x,y)]}{\sqrt{\Lambda_{\sigma q}}},$$

$$\Upsilon_{\tau q}^{(5)}(x,y) = \frac{j_{\tau}[\kappa R(x,y)]}{S(x,y)} \frac{Q_{\tau}^q[C(x,y)]}{\sqrt{\Lambda_{\tau q}}},$$

$$\Upsilon_{\sigma q}^{(6)}(x,y) = C(x,y) \frac{j_{\sigma}[\kappa R(x,y)]}{\kappa R(x,y)} \frac{P_{\sigma}^q[C(x,y)]}{\sqrt{\Lambda_{\sigma q}}},$$

$$\Upsilon_{\sigma q}^{(7)}(x,y) = D_{\sigma}[\kappa R(x,y)] \frac{Q_{\sigma}^q[C(x,y)]}{\sqrt{\Lambda_{\sigma q}}},$$

$$\Upsilon_{\tau q}^{(8)}(x,y) = j_{\tau}[\kappa R(x,y)]\frac{P_{\tau}^{q}[C(x,y)]}{\sqrt{\Lambda_{\tau q}}},$$

and

$$R(x,y) = \sqrt{(x\rho_d)^2 + (yh_d + a)^2},$$

$$S(x,y) = \frac{x\rho_d}{\sqrt{(x\rho_d)^2 + (yh_d + a)^2}},$$

$$C(x,y) = \frac{yh_d + a}{\sqrt{(x\rho_d)^2 + (yh_d + a)^2}}.$$

*ruhlenko_ivan@mail.ru

[1] D. Courjon and C. Bainier, Rep. Prog. Phys. **57**, 989 (1994).
[2] L. Novotny and S. J. Stranick, Annu. Rev. Phys. Chem. **57**, 303 (2006).
[3] A. Bouhelier, M. R. Beversluis, and L. Novotny, Ultramicroscopy **100**, 413 (2004).
[4] E. J. Sanchez, L. Novotny, and X. S. Xie, Phys. Rev. Lett. **82**, 4014 (1999).
[5] J. Wessel, J. Opt. Soc. Am. B **2**, 1538 (1985).
[6] A. Bek, R. Vogelgesang, and K. Kern, Rev. Sci. Instrum. **77**, 043703 (2006).
[7] J. M. Gerton, L. A. Wade, G. A. Lessard, Z. Ma, and S. R. Quake, Phys. Rev. Lett. **93**, 180801 (2004).
[8] R. Hillenbrand and F. Keilmann, Appl. Phys. Lett. **80**, 25 (2002).
[9] R. Hillenbrand and F. Keilmann, Phys. Rev. Lett. **85**, 3029 (2000).
[10] S. Gresillon, H. Cory, J. C. Rivoal, and A. C. Boccara, J. Opt. A, Pure Appl. Opt. **1**, 178 (1999).
[11] B. Knoll and F. Keilmann, Nature (London) **399**, 134 (1999).
[12] R. Hillenbrand and F. Keilmann, Appl. Phys. B: Lasers Opt. **73**, 239 (2001).
[13] Y. C. Martin, H. F. Hamann, and H. K. Wickramasinghe, J. Appl. Phys. **89**, 5774 (2001).
[14] J. Aizpurua, S. P. Apell, and R. Berndt, Phys. Rev. B **62**, 2065 (2000).
[15] A. V. Goncharenko, J.-K. Wang, and Y.-C. Chang, Phys. Rev. B **74**, 235442 (2006).
[16] J. Jersch, F. Demming, L. J. Hildenhagen, and K. Dickmann, Appl. Phys. A: Mater. Sci. Process. **66**, 29 (1998).
[17] R. M. Roth, N. C. Panoiu, M. M. Adams, R. M. Osgood, C. C. Neacsu, and M. B. Raschke, Opt. Express **14**, 2921 (2006).
[18] S. Nie and S. R. Emory, Science **275**, 1102 (1997).
[19] A. Kramer, W. Trabesinger, B. Hecht, and U. P. Wild, Appl. Phys. Lett. **80**, 1652 (2002).
[20] A. Bouhelier, M. Beversluis, A. Hartschuh, and L. Novotny, Phys. Rev. Lett. **90**, 013903 (2003).
[21] B. Knoll and F. Keilmann, Opt. Commun. **182**, 321 (2000).
[22] J. R. Zurita-Sanchez and L. Novotny, J. Opt. Soc. Am. B **19**, 1355 (2002).
[23] E. Moreno, D. Erni, C. Hafner, and R. Vahldieck, J. Opt. Soc. Am. A **19**, 101 (2002).
[24] L. Novotny, R. X. Bian, and X. S. Xie, Phys. Rev. Lett. **79**, 645 (1997).
[25] C. Hafner, *The Generalized Multiple Multipole Technique for Computational Electromagnetics* (Artech, Boston, 1990).
[26] O. J. F. Martin, C. Girard, and A. Dereux, Phys. Rev. Lett. **74**, 526 (1995).
[27] A. L. Demming, F. Festy, and D. Richards, J. Chem. Phys. **122**, 184716 (2005).
[28] J. T. Krug, E. J. Sanchez, and X. S. Xie, J. Chem. Phys. **116**, 10895 (2002).
[29] A. V. Goncharenko, H.-C. Chang, and J.-K. Wang, Ultramicroscopy **107**, 151 (2007).
[30] A. V. Goncharenko, M. M. Dvoynenko, and H.-C. Chang, Appl. Phys. Lett. **88**, 104101 (2006).
[31] I. Notingher and A. Elfick, J. Phys. Chem. B **109**, 15699 (2005).
[32] P. Johansson, S. P. Apell, and D. R. Penn, Phys. Rev. B **64**, 054411 (2001).
[33] M. Idemen, Wave Motion **38**, 251 (2003).
[34] R. M. Feenstra, J. Vac. Sci. Technol. B **21**, 2080 (2003).
[35] Y. Kawata, C. Xu, and W. Denk, J. Appl. Phys. **85**, 1294 (1999).
[36] W. Denk and D. W. Pohl, J. Vac. Sci. Technol. B **9**, 510 (1991).
[37] L. Banyai and S. W. Koch, *Semiconductor Quantum Dots* (World Scientific, Singapore, 1993), Vol. 2.
[38] G. W. Bryant, J. Lumin. **70**, 108 (1996).
[39] *Semiconductor Quantum Dots. Physics, Spectroscopy and Applications*, edited by Y. Masumoto and T. Takagahara (Springer, Berlin, 2002).
[40] L. Klinkenbusch, Arch. Elektrotech. (Berlin) **76**, 181 (1993).
[41] *Optics of Nanostructures*, edited by A. V. Fedorov (Nedra, Saint-Petersburg, 2005).
[42] D. Bimberg, M. Grundmann, and N. N. Ledentsov, *Quantum Dot Heterostructures* (Wiley, New York, 1999).
[43] A. V. Fedorov, A. V. Baranov, and K. Inoue, Phys. Rev. B **54**, 8627 (1996).
[44] L. He, G. Bester, Z. Su, and A. Zunger, Phys. Rev. B **76**, 035313 (2007).
[45] F. M. Huang, F. Festy, and D. Richards, Appl. Phys. Lett. **87**, 183101 (2005).
[46] K. Matsuda, T. Saiki, S. Nomura, M. Mihara, Y. Aoyagi, S. Nair, and T. Takagahara, Phys. Rev. Lett. **91**, 177401 (2003).
[47] K. Matsuda, T. Saiki, S. Nomura, M. Mihara, and Y. Aoyagi, Appl. Phys. Lett. **81**, 2291 (2002).
[48] D. Hessman, J. Persson, M.-E. Pistol, C. Pryor, and L. Samuelson, Phys. Rev. B **64**, 233308 (2001).
[49] V. Zwiller, L. Jarlskog, M.-E. Pistol, C. Pryor, P. Castrillo, W. Seifert, and L. Samuelson, Phys. Rev. B **63**, 233301 (2001).
[50] H. Pettersson, C. Pryor, L. Landin, M.-E. Pistol, N. Carlsson, W. Seifert, and L. Samuelson, Phys. Rev. B **61**, 4795 (2000).
[51] R. Heitz, M. Veit, N. N. Ledentsov, A. Hoffmann, D. Bimberg, V. M. Ustinov, P. S. Kop'ev, and Z. I. Alferov, Phys. Rev. B **56**, 10435 (1997).
[52] R. Heitz *et al.*, Appl. Phys. Lett. **68**, 361 (1996).
[53] M. J. Steer, D. J. Mowbray, W. R. Tribe, M. S. Skolnick, M. D. Sturge, M. Hopkinson, A. G. Cullis, C. R. Whitehouse, and R. Murray, Phys. Rev. B **54**, 17738 (1996).
[54] K. H. Schmidt, G. Medeiros-Ribeiro, M. Oestreich, P. M. Petroff, and G. H. Döhler, Phys. Rev. B **54**, 11346 (1996).

[55] E. L. Ivchenko and G. E. Pikus, *Superlattices and Other Heterostructures* (Springer, Berlin, 1997), Vol. 110.
[56] K. Blum, *Density Matrix: Theory and Applications* (Plenum, New York, 1981).
[57] M. Cardona, *Light Scattering in Solids II*, Topics in Applied Physics, Vol. 50 (Springer-Verlag, Heidelberg, 1982), Chap. 2.
[58] A. V. Fedorov, A. V. Baranov, I. D. Rukhlenko, and S. V. Gaponenko, Phys. Rev. B **71**, 195310 (2005).
[59] A. V. Fedorov, A. V. Baranov, I. D. Rukhlenko, and Y. Masumoto, Solid State Commun. **128**, 219 (2003).
[60] X.-Q. Li and Y. Arakawa, Phys. Rev. B **57**, 12285 (1998).
[61] T. Inoshita and H. Sakaki, Physica B **227**, 373 (1996).
[62] P. C. Sercel, Phys. Rev. B **51**, 14532 (1995).
[63] A. L. Efros, V. A. Kharchenko, and M. Rosen, Solid State Commun. **93**, 281 (1995).
[64] U. Bockelmann and T. Egeler, Phys. Rev. B **46**, 15574 (1992).
[65] T. Inoshita and H. Sakaki, Phys. Rev. B **46**, 7260 (1992).
[66] U. Bockelmann and G. Bastard, Phys. Rev. B **42**, 8947 (1990).
[67] C. F. Bohren and D. R. Huffman, *Absorption and Scattering of Light by Small Particles* (Wiley, New York, 1983).